




NO₂ and NH₃ detection using work function measurement of solvothermal synthesised ZnO–NiO nanocomposites: a case study

Deepak Goyal³, Chandra Prakash Goyal^{1,2}, David Chidambaram¹, Yuvaraj Sivalingam¹, Hiroya Ikeda², S. Ponnusamy¹, and Niranjana S. Ramgir^{3,*} 

¹Department of Physics and Nanotechnology, SRM Institute of Science and Technology, Kattankulathur, Tamil Nadu 603 203, India

²Graduate School of Science and Technology, Shizuoka University, Hamamatsu 432 8011, Japan

³Technical Physics Division, Bhabha Atomic Research Centre, Mumbai 400 085, India

Received: 15 February 2024

Accepted: 28 April 2024

© The Author(s), 2024

ABSTRACT

Work function measurement using Kelvin probe method has been demonstrated as an effective and novel approach towards detection of NH₃ and NO₂ gases using ZnO–NiO based nanocomposites. For this the nanocomposites were synthesised in different compositions using the solvothermal method. Formation of ZnO–NiO nanocomposites was confirmed using XRD and EDS studies. It is found that the nanoparticle morphology of NiO changes with different percentages of Zn addition. The work function of the sensing film was found to decrease and increase upon exposure to NH₃ (1.51) and NO₂ (1.18) gases owing to the reducing and oxidising nature of the test gases. Of the different composites, Zn_{0.75}Ni_{0.25}O exhibited highest sensor response towards the test gases. The increased response is attributed to the nanostructured morphology of the nanocomposite and the formation and collapse of the p–n heterojunction formed between p-type NiO and n-type ZnO. Besides, incorporation of NiO enhances the oxygen adsorption on the sensor surface assigned to the Ni²⁺ ions getting readily oxidised to Ni³⁺. Our results clearly suggest that the work function measurements could also be used as an effective way for NO₂ and NH₃ detection.

1 Introduction

Air pollution has recently emerged as the most serious environmental issue [1]. Of the various pollutants, ammonia (NH₃) and nitrogen dioxide (NO₂) are useful for numerous industries such as fertiliser, pesticides,

petrochemical, chemical and medical [2–4]. NH₃ is a colourless, highly hazardous gas and the Occupational Safety and Health Administration (OSHA) has set an exposure limit of 50 ppm [5]. Above this, it leads to various health issues such as headaches, difficulty breathing, and vomiting. In the similar context, NO₂

Deepak Goyal and Chandra Prakash Goyal have contributed equally to this work.

Address correspondence to E-mail: niranjanpr@yahoo.com

<https://doi.org/10.1007/s10854-024-12685-3>

Published online: 14 May 2024

is highly toxic and responsible for acid rain and its exposure limit is set to 5 ppm [6]. For higher concentrations, it damages the human respiratory tract and could be fatal.

These gases have been monitored using several methods including optical [7], electrochemical [8], work function [9], chemiresistive [10], gas chromatography (GC), and mass spectroscopy [11]. Some of these techniques are sophisticated, expensive, and time-consuming. Among these, chemiresistive-based gas sensors are more popular in the current scenario. These sensors rely on the direct chemical interaction between the analyte species and sensing material. They are easy to use, durable, eco-friendly and cost effective. For this, several metal oxide semiconductor (MOS) nanomaterials such as ZnO, SnO₂, NiO, and TiO₂ have been studied [12–15]. The sensing materials have been realized using different chemical methods, such as hydrothermal [16], wet chemical route [17] and solvothermal [18]. Among them, the solvothermal technique offers the advantage of being eco-friendly and accordingly, is commercially exploited for the synthesis of well-defined nano-morphologies [19]. Of the different MOS, ZnO, having a wide band gap of 3.3 eV and a large exciton binding energy of 60 meV [20], is considered to be a suitable candidate for gas sensing application.

ZnO is n-type in nature and has some unique properties like biocompatibility, good electron mobility, thermal and chemical stability. Another semiconductor material, NiO is p-type in nature, has wide band gap of 3.7 eV and exhibit good electrical, chemical, and

thermal stability. It also show good catalytic properties to oxidize metal oxides [21]. Thus, use of ZnO and NiO together is anticipated to form random nano heterojunction namely p-n junctions and thereby could show enhanced sensing responses. Table 1 compares responses of different ZnO/NiO-based nano-heterostructures towards different gases. The observed improved response kinetics have been attributed predominantly to the unique interaction with the test gases resulting in subsequent collapse and formation of p-n junctions resulting in a drastic change in electric properties thereby a higher sensor response [22]. The nanocomposites are investigated for their response towards different gases using chemiresistive principles. The chemical interaction on the sensor surface results in the large change in the resistance which is measured and calibrated with respect to gas concentration. As is evident from the Table 1, the ZnO/NiO heterostructure system has been explored for sensor towards gases like H₂S, SO₂, acetone and toluene. The heterostructure system has been rarely reported for the NO_x detection. For example. Dong et al., investigated the litchi shell-like porous NiO/ZnO composite film realised using electrodeposition method for its response towards NO_x at room temperature. The sensor film exhibited a response of 74.0% towards 100 ppm of NO_x gas [23]. Similarly, NiO coated ZnO films realized using chemical bath deposition method has also been reported for the NO₂ sensing by Mane et al. [24]. The sensor film exhibited a response of 76.5% towards 100 ppm of NO₂ at moderate working temperature of 150 °C.

Table 1 Different ZnO/NiO nanocomposite based gas sensors

Material	Technique	Morphology	Analyte	Conc. (ppm)	SR/T (°C)	References
ZnO-Al	Hydrothermal	NW	NO ₂	4	6.2/230	[41]
NiO	Hydrothermal	NP	(CH ₃) ₂ CO	100	0.25/300	[47]
ZnO/NiO	Wet-chemical	Core shell	(CH ₃) ₂ CO	500	NA/300	[48]
ZnO/NiO	Co-sputtering	Thin film	C ₂ H ₆ O	100	5.4/300	[49]
ZnO/NiO	Electro-spinning	Multi-junction grains	(CH ₃) ₂ CO	100	6/25	[50]
ZnO/NiO	Hydrothermal	NW	H ₂ S	100	0.31/25	[51]
ZnO/NiO	Hydrothermal	Nano disk	SO ₂	50	28/240	[52]
ZnO/NiO	Chemical	Litchi shell	NO _x	100	0.74/25	[23]
ZnO/NiO	Co-precipitation	Microspheres	Toluene	100	240/300	[53]
ZnO/NiO	Hydrothermal	Nanodisks	SO ₂	20	16.25/240	[54]
ZnO/NiO	Green method	Nanocubes	LPG	2.5 vol.%	7.72/32	[55]
ZnO/NiO	Hydrothermal	3D NW network	Ethylene glycol	100	58.87/175	[56]

SR sensor response, NW nanowires, NP nanoparticles, LPG liquified petroleum gas

Thus, the formation and collapse of p–n junction upon interaction with the test gases have been found to be the predominant process for the observed large change in the sensor response. This large change in the resistance means more electrons are crowding the Fermi level of the material, and subsequently can cause a drastic variation in the Fermi level position of the work function of the material. This change in work function can be measured and could be used as an alternate approach to the chemiresistive principle. Kelvin probe method is the well-established technique to measure the work function of the material. Usually, the work function has surface band bending and electron affinity components associated with it and is given as;

$$\phi = qV_s + \chi \quad (1)$$

Here, qV_s is the surface band bending and χ is the electron affinity [25, 26]. Interaction on the sensor surface causes changes in work function owing to variation in both surface band bending and electron affinity (a measure of surface dipole moment) [27, 28]. For n-type material, surface band bending or heterojunction barrier is measured by calculating the resistance changes given as;

$$q\Delta V_s = kT \ln \left(R_g/R_a \right) \quad (2)$$

For p-type it is given as;

$$q\Delta V_s = -2kT \ln \left(R_g/R_a \right) \quad (3)$$

where, R_a and R_g are the resistances before and after exposure to oxidising gas, q is the electronic charge, k is the Boltzmann constant and T is the absolute temperature. From Eqs. (1) and (3), it is clearly evident that the chemical interactions occurring on the sensor surface results in surface band bending which is reflected as the corresponding change in the work function of the material [29]. This change can thus be measured using Kelvin probe studies and be used as an alternate approach or supplementary technique for gas sensing studies.

Accordingly, in the present work, we report the Kelvin probe method as an alternative approach for gas sensing studies. More specifically, work function variations observed during interaction of NH_3 and NO_2 gases with the sensor surface of ZnO–NiO nanocomposite synthesised using solvothermal method is demonstrated as a technique for the evaluation of

gas sensing properties. For this, first the nanocomposite with different compositions were synthesised and tested to find the optimum configuration that can result in maximum change in the work function. Our results clearly demonstrate that the work function can be used as a supplementary technique to chemiresistive one for the detection of toxic gases.

2 Experimental

2.1 Synthesis of pristine NiO and ZnO–NiO nanocomposite

For NiO nanostructure synthesis, NiNO_3 and urea were dissolved in a mixture of isopropyl alcohol (IPA) and glycerol. This solution was transferred into an autoclave, and the solvothermal process was performed at 180 °C for 24 h in a muffle furnace. Synthesized precipitates were centrifuged and dried in an oven. For ZnO incorporation, ZnNO_3 was added to the starting solution in different molar ratios. Prepared samples were labelled as S1, S2, S3, S4, S5, and S6 based on nickel and zinc atomic percentage (at. %) ratios of NiO, $\text{Ni}_{0.67}\text{Zn}_{0.33}\text{O}$, $\text{Ni}_{0.50}\text{Zn}_{0.50}\text{O}$, $\text{Ni}_{0.33}\text{Zn}_{0.67}\text{O}$, $\text{Ni}_{0.25}\text{Zn}_{0.75}\text{O}$ and ZnO, respectively, as measured by EDS. The prepared samples were calcinated in an air atmosphere at 450 °C for 2 h in a furnace. Sensor films (30 μm thick) were prepared on glass substrates using the doctor-blades coating method. The scanning Kelvin probe was used to measure the contact potential difference (CPD) of the prepared films. To investigate the effect of gas interaction, the sensor film was exposed to NO_2 (50 ppm) at 150 °C with subsequent quenching to room temperature arresting the chemical interactions occurring on the sensor surface. The contact potential difference (CPD) was recorded before and after exposure to NO_2 and NH_3 gases and correlated to understand the effect on the work function of the sensing material.

2.2 Characterization techniques

X-ray diffraction (XRD) studies were carried out on a RINT2200 X-ray diffractometer (Rigaku Corporation, Tokyo, Japan) with a Cu-K_α radiation source ($\lambda = 1.54 \text{ \AA}$). Surface morphology of the synthesized samples were inspected using field emission scanning electron microscope (FESEM) JEOL JSM-7001F at an accelerating voltage of 15 kV. Elemental compositions

were measured by energy dispersive X-ray spectroscopy (EDS) using EDAX APOLLO X, AMETEK Co. Limited, Tokyo, Japan. X-ray photoelectron spectroscopy (XPS) studies were performed using Al-K α radiation and Shimadzu Axis Ultra DLD, Shimadzu Corporation, Kyoto, Japan. Scanning Kelvin probe technique (SKP) was used to measure the contact potential difference (CPD) of prepared films [30, 31]. CPD were recorded before and after gas exposure. CPD (ϕ) (in meV) is estimated using equation;

$$\phi = 5100 - \text{CPD}_{\text{Au}} + \text{CPD}_{\text{sample}} (\text{meV}) \quad (4)$$

where, 5100 denotes the work function of gold in meV, CPD_{Au} denotes the CPD between the tip and the gold-coated reference sample, and $\text{CPD}_{\text{sample}}$ denotes the CPD between the tip and the sample. All measurements were performed at room temperature. The average value of CPD was determined by raster scanning the tip across a 4 mm² area of the sample surface. To determine the effect of gas exposure on sensor films, work function measurements were performed before and after exposure to 50 ppm of gases at 150 °C followed by sudden quenching to room temperature.

3 Results and discussion

3.1 Structural optical and morphological characterization

XRD investigation of prepared samples confirmed the formation of ZnO–NiO composites, as shown in Fig. 1. Sample S1 show peaks at 37.3, 43.36, 63.08, 75.50, and

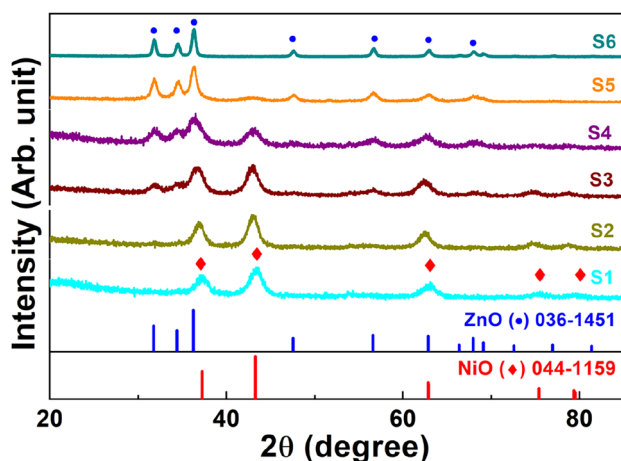


Fig. 1 XRD plot for different ZnO–NiO composites

79.37 corresponding to (101), (012), (104), (113), and (202) diffraction planes that matched well with the JCPDS data of the cubic phase of NiO crystal structure (044-1159) [32]. Sample S6 shows XRD peaks at 31.82, 34.50, 36.32, 47.60, 56.68, 62.94, and 67.98, which correspond to (100), (002) (101), (102), (110), (103) and (112) diffraction planes of the wurtzite hexagonal ZnO crystal structure matching with the JCPDS data (036-1451). In samples S2–S5, both NiO and ZnO have co-existed with relative intensity of the ZnO peaks increasing from S2 to S5. In the S5 sample, the peak at 43.36 has disappeared, and some peaks have appeared at 31.82, 34.50, 47.60, and 56.68. Peak shift and peak broadening with extra peaks related to ZnO were observed with an increase in Zn content. Elemental percentages analysed by EDS analysis were found to be the same as those used during synthesis, as mentioned in Table 2. Elemental composition of the sample indicate Zn, O, and Ni elements are uniformly distributed in the samples. The relative increase in the intensity is in accordance to the XRD results.

The morphologies of pure NiO, ZnO, and ZnO/NiO nanocomposite samples were studied using FE-SEM. Synthesised samples (S1–S4) showed rock-like nanostructures of 200–300 nm (Fig. 2). Pure ZnO (S6) showed a larger spherical structure of 2–3 μm in size. Sample S5 showed porous nanostructured morphology with a smallest size of 20–80 nm and a high surface area, which is useful for gas sensor applications. Elemental mapping of S5 confirmed the uniform distribution of Zn, Ni, and O and the formation of ZnO–NiO composites without any segregation (Fig. 3). Further chemical composition change and oxidation states of NiO/ZnO nanocomposite have been studied using XPS analysis.

XPS studies were performed for samples S5 and S6, as shown in Fig. 4. Pure ZnO (S6) showed

Table 2 Elemental composition as analysed for all the samples using EDS

Sample code	Composition (at. %)		
	Ni	Zn	O
S1	35.62	-	64.38
S2	38.60	17.62	43.77
S3	28.30	26.33	45.38
S4	23.42	33.90	42.67
S5	11.36	32.07	56.57
S6	-	65.78	34.22

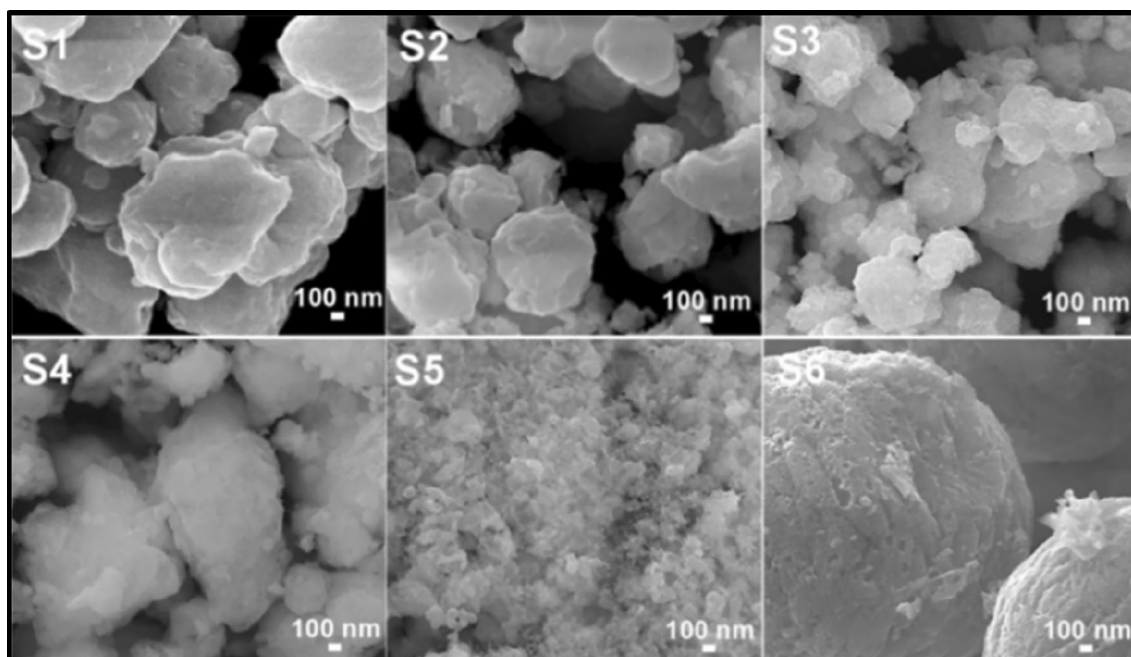


Fig. 2 SEM images of all prepared ZnO–NiO composite

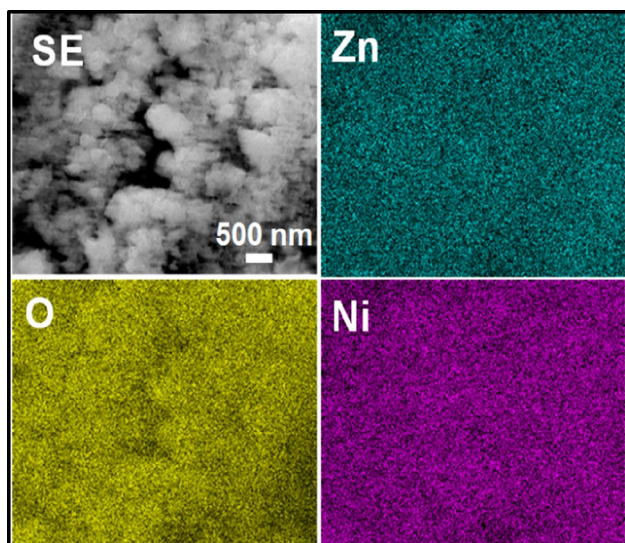


Fig. 3 Elemental mapping for S5 sample

characteristic peaks for Zn 2p at binding energy (BE) values of 1021.28 and 1044.35 eV, corresponding to $2p_{3/2}$ and $2p_{1/2}$, respectively [33, 34]. O1s spectra showed peaks at 531.20 and 530.05 eV for adsorbed oxygen and lattice oxygen species, respectively [35]. In the XPS spectra for S5, after Ni incorporation (S5), a Zn 2p spectrum was slightly shifted to lower BE due to the ZnO–NiO interaction. Two sharp peaks situated

at 1020.08 and 1043.08 eV correspond to the Zn $2p_{3/2}$ and Zn $2p_{1/2}$ states, respectively [36]. O1s spectra show peaks at 531.20 and 530.05 eV for adsorbed oxygen and lattice oxygen species, respectively [35]. An extra peak at 528.34 eV was observed in the O 1s spectra, which corresponds to the surface chemisorbed oxygen of the ZnO/NiO nanocomposite sample [37, 38]. The sample S5 showed a higher oxygen percentage compared to S6, which is helpful for gas sensing. The XPS spectra for Ni have shown four different BE peaks at 855.1/861.2 eV and 873.1/879.2 eV, corresponding to Ni $2p_{3/2}$ and Ni $2p_{1/2}$, respectively [39]. The spin-energy separation of 18 eV supports the existence of Ni^{2+} ions in NiO [40]. For Sample S5, the Ni 2p spectra matches well with the reported values and confirms the presence of Ni as NiO.

3.2 Gas sensing studies using work function measurements

Work function (ϕ) was measured for all the prepared samples by Kelvin probe measurements, as shown in Fig. 5a. Work function was found to decrease with an increase in Zn percentage which can be attributed to the n-type characteristics of ZnO and corresponding shift in Fermi level towards upward directions. Of the different samples, S2 sample showed maximum increase in the work function and is assigned

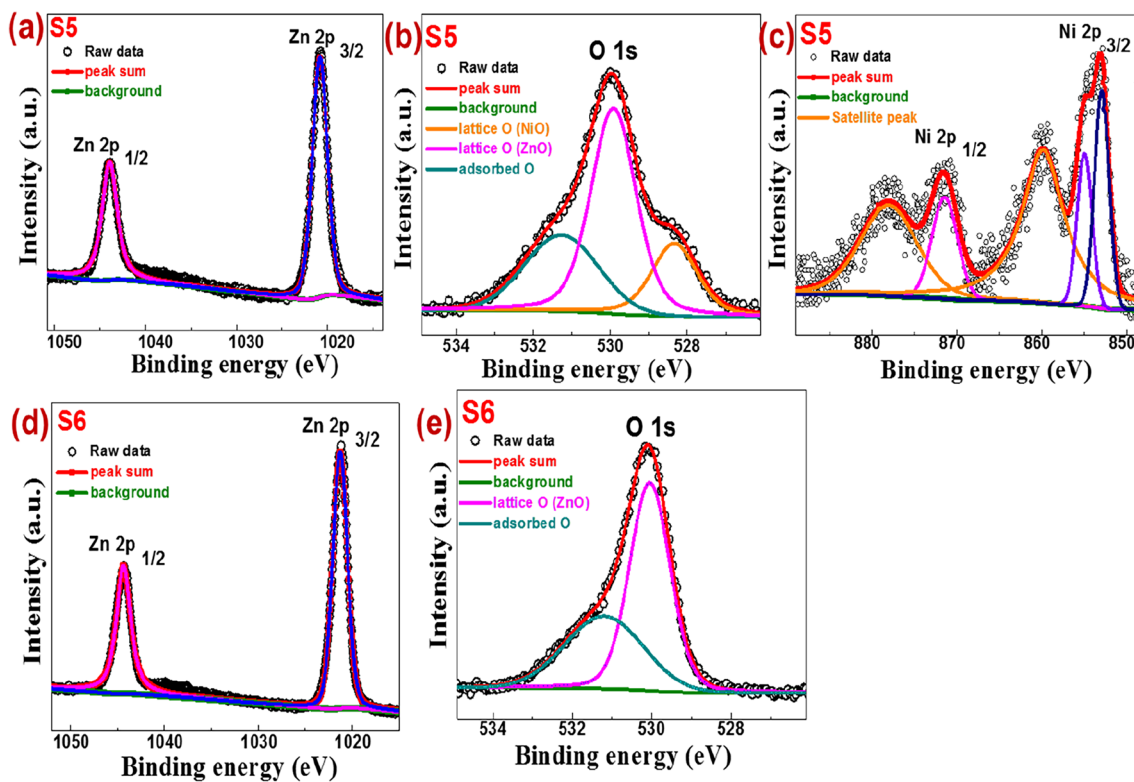
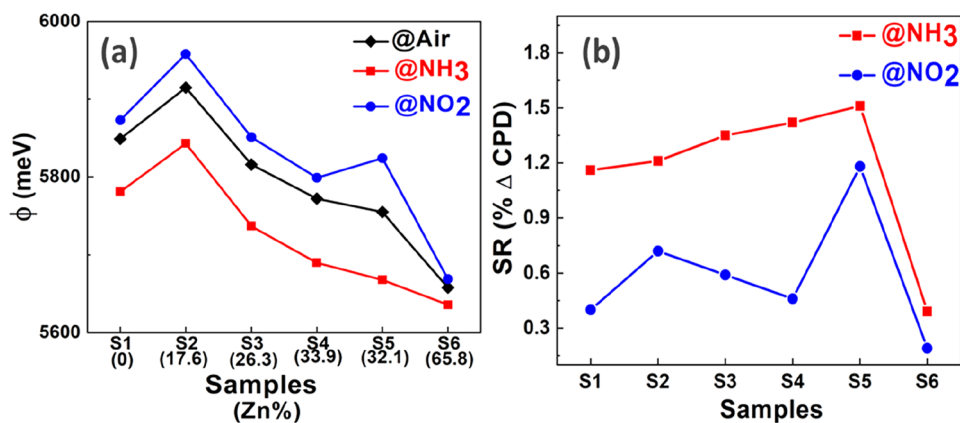


Fig. 4 XPS spectra for sample S5 and S6

Fig. 5 **a** Work function (meV) as a function of Zn percentage and **b** percentage of CPD change, for all samples



to the creation of larger defect states and vacancies. Now, NO₂ being oxidising in nature, all samples exhibited an increase in work function after exposure, with corresponding downward shift in Fermi level [41]. In the case of NH₃, which being reducing in nature, a decrease in the work function owing to upward shift in Fermi level is observed [42]. The sensor response (SR) was calculated as a percentage change in CPD before and after gas exposure and is depicted in Fig. 5b. It was observed that the response

to gas, increased with an increase in Zn content for all ZnO–NiO nanocomposite samples. But in the case of pure ZnO (S6), the response decreased due to no heterostructure barrier formation and larger particle size. All the samples showed a higher response to NH₃ compared to NO₂. The sensor response of the S5 sample has shown a higher value due to higher porosity and more adsorbed oxygen species nanoparticles, which were confirmed by SEM, EDS, and XPS analysis, respectively.

The work function 3D area scan plot for sample S5 is shown in Fig. 6a. Work function was found to be almost constant throughout the surface. For the S5 sample, work function was found to decrease with NH₃ gas exposure and increase when the same sample is exposed to NO₂ gas. *I*–*V* measurements were performed with and without gas to confirm the semiconducting nature of the S5 sample, as shown in Fig. 6b. The slope of the *I*–*V* plot (1/*R*) decreased after NH₃ exposure and vice versa in the case of NO₂.

A gas sensing mechanism is proposed in Fig. 7 to explain our sensing results. The interfaces of NiO (p-type) and ZnO (n-type) combine to form a p-n

heterojunction with a built-in potential related to the extent of interaction or the respective percentage of individual in the nanocomposite [43]. Formation of ZnO–NiO composites leads to the band bending and an increase in the depletion region thereby lowering of the Fermi level or increase in the resistance of the sensing film (Fig. 7a). Herein, electron transfer takes place from ZnO to NiO while holes are transferred from NiO to ZnO till the equilibrium is reached. Besides, NiO modification results in the adsorption of more oxygen ions on the sensor surface due to its catalytic activity and Ni²⁺ ions getting readily oxidised to Ni³⁺ [44]. Now, upon exposure, NH₃ interacts with the increased adsorbed

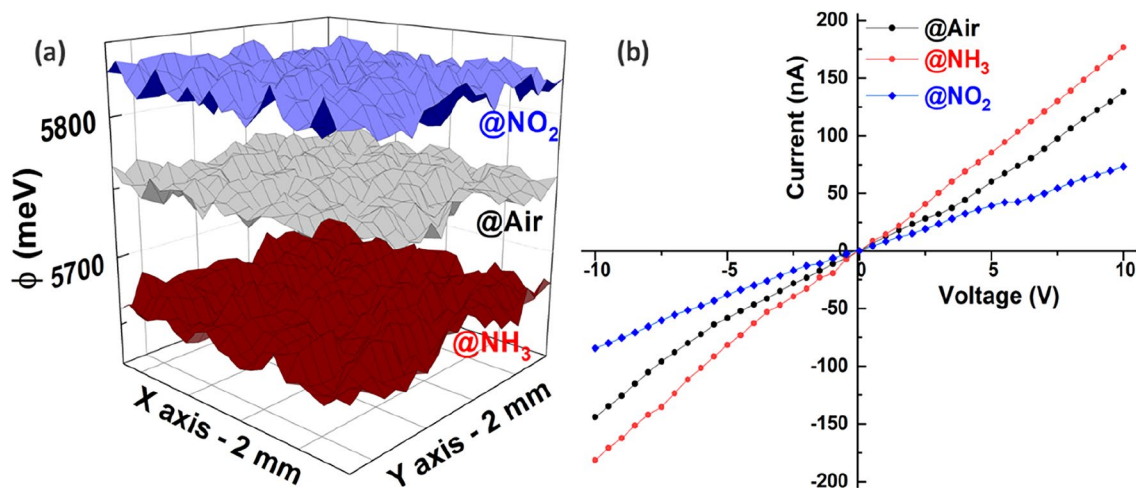
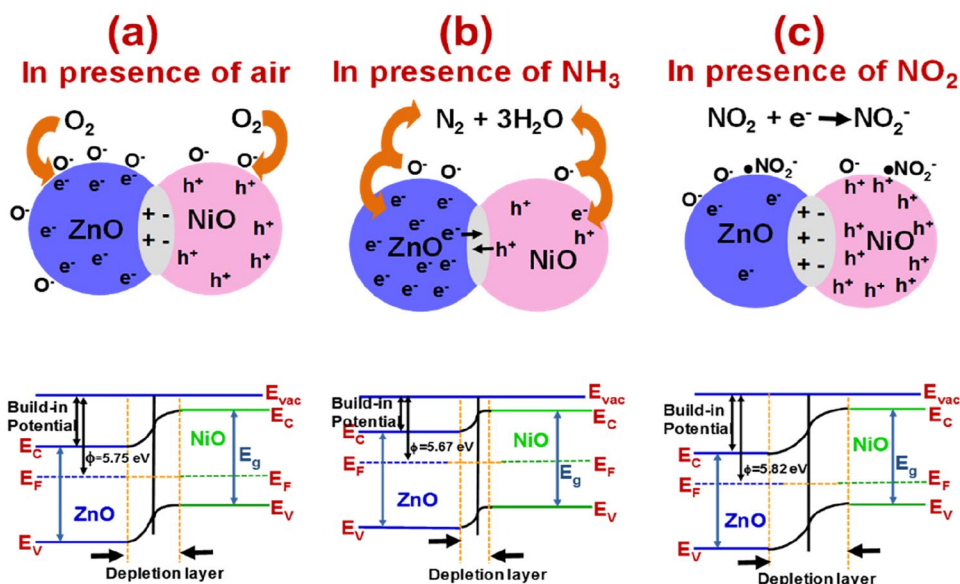
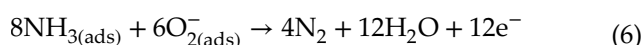


Fig. 6 a 3D work function and b *I*–*V* characteristics graph of S5 with and without gases

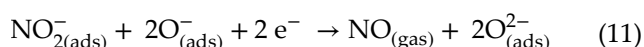
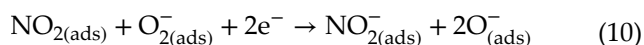
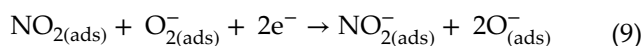
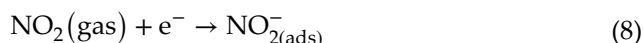
Fig. 7 Gas sensing mechanism for ZnO–NiO composites



surface oxygen causing oxidation of the ammonium gas molecules into N_2 and H_2O (Fig. 7b) [42]. This results in the release of the trapped electrons back to the sensor film. This eventually causes a decrease in the depletion region of the p–n junction which is reflected as the increase in the Fermi level or lower resistance of the sensing film. The corresponding reactions on the sensor surface are explained in Eqs. (5) and (6) below [35];



Upon exposure (Fig. 7c), NO_2 interacts with the adsorbed oxygen species present on the surface by taking up or capturing electrons from the conduction band of the sensing material. This causes an increase in the resistance of the sensing film thereby widening of the depletion region of the p–n junction. The interactions on the sensor surface are explained in the following Eqs. (7), (8), (9), and (10) below [45];



Work function measurements of ZnO–NiO system using KP method has also been reported in the literature. For ZnO and ZnO_{NR}/NiO core shell heterostructures, ϕ of 4.42 and 4.70 eV, respectively in the dark conditions is reported [46]. Herein also, an increase in ϕ due to modification of NR surface by NiO is observed. This has been attributed to the formation of heterostructure in particular p–n junction further corroborating our results.

4 Conclusion

Monodispersed uniform NiO was successfully synthesised using the solvothermal technique at 180 °C for 24 h. ZnO was added to the NiO solution in different molar ratios to make different compositions of the nanocomposite. The compositional, structural, work function and electrical properties of ZnO–NiO were thoroughly studied. All of the samples responded more strongly to NH_3 than to NO_2 gas. The maximum change in the work function or the highest sensor response was calculated for sample S5 for NH_3 (1.51) and NO_2 (1.18) gases, which was due to small size nanoparticles as also investigated using the SEM study. Of the different compositions, Zn_{0.75}Ni_{0.25}O nanocomposite exhibited good sensing response and associated better p–n heterojunction interface as compared to another nanocomposite composition. Thus, our results clearly demonstrate work function studies using Kelvin probe method to be an excellent alternative to Chemiresistive sensors for gas sensing.

Acknowledgements

We are grateful to SRMIST for providing research facilities and infrastructure. The authors also acknowledge the Centre for Instrumental Analysis, Shizuoka University, Japan, for providing characterization facilities. Deepak Goyal thanks the Department of Science and Technology, Government of India, for providing the Inspire fellowship (INSPIRE Reg. No. IFA22-ENG341).

Author contributions

Deepak Goyal: Conceptualization; data curation; formal analysis, original draft; methodology; software; Chandra Prakash Goyal: Conceptualization; data curation; formal analysis, original draft; methodology; software; David Chidambaram: Data curation; characterization. Yuvaraj Sivalingam: Data curation; characterization. Hiroya Ikeda: Formal analysis, characterization, resources, S. Ponnusamy: Formal analysis, resources, supervision; N. S. Ramgir: Conceptualization; methodology; writing—review and editing, supervision.

Funding

Open access funding provided by Department of Atomic Energy. Funding was provided by DST, New Delhi (INSPIRE Reg. No. IFA22-ENG341).

Data availability

The datasets generated during and/or analysed during the current study are available from the corresponding author on reasonable request.

Declarations

Conflict of interest The authors declare no conflict of interest. We did not have known competing financial interests or personal relationships that could have appeared to influence the work reported in this paper.

Open Access This article is licensed under a Creative Commons Attribution 4.0 International License, which permits use, sharing, adaptation, distribution and reproduction in any medium or format, as long as you give appropriate credit to the original author(s) and the source, provide a link to the Creative Commons licence, and indicate if changes were made. The images or other third party material in this article are included in the article's Creative Commons licence, unless indicated otherwise in a credit line to the material. If material is not included in the article's Creative Commons licence and your intended use is not permitted by statutory regulation or exceeds the permitted use, you will need to obtain permission directly from the copyright holder. To view a copy of this licence, visit <http://creativecommons.org/licenses/by/4.0/>.

References

1. S. Dhall, B.R. Mehta, A.K. Tyagi, K. Sood, *Sensors Int.* (2021). <https://doi.org/10.1016/j.sintl.2021.100116>
2. D. Kwak, Y. Lei, R. Maric, *Talanta* (2019). <https://doi.org/10.1016/j.talanta.2019.06.034>
3. N.P. Cheremisinoff, P.E. Rosenfeld, *Handbook of Pollution Prevention and Cleaner Production Vol. 3: Best Practices in the Agrochemical Industry* (2010). <https://doi.org/10.1016/C2009-0-20362-X>
4. A. Amaducci, J.W. Downs, *Nitrogen Dioxide Toxicity* (2020)
5. OSHA, *All About Occupational Safety and Health Administration (OSHA)*, U.S. Dep. Labor. (2016)
6. Z. Zhang, M. Haq, Z. Wen, Z. Ye, L. Zhu, *Appl. Surf. Sci.* (2018). <https://doi.org/10.1016/j.apsusc.2017.10.074>
7. H.E. Joe, H. Yun, S.H. Jo, M.B.G. Jun, B.K. Min, *Int. J. Precis. Eng. Manuf.* (2018). <https://doi.org/10.1007/s40684-018-0017-6>
8. T. Liu, X. Wang, L. Li, J. Yu, *J. Electrochem. Soc.* (2017). <https://doi.org/10.1149/2.0501713jes>
9. P. Bondavalli, P. Legagneux, D. Pribat, *Sens. Actuators B* (2009). <https://doi.org/10.1016/j.snb.2009.04.025>
10. N. Joshi, T. Hayasaka, Y. Liu, H. Liu, O.N. Oliveira, L. Lin, *Microchim. Acta* (2018). <https://doi.org/10.1007/s00604-018-2750-5>
11. K. Lamote, P. Brinkman, L. Vandermeersch, M. Vynck, P.J. Sterk, H. Van Langenhove, O. Thas, J. Van Cleemput, K. Nackaerts, J.P. Van Meerbeeck, *Oncotarget.* (2017). <https://doi.org/10.18632/oncotarget.21335>
12. K.G. Krishna, G. Umadevi, S. Parne, N. Pothukanuri, *J. Mater. Chem. C.* (2023). <https://doi.org/10.1039/d2tc04690c>
13. B. Bhangare, K.R. Sinju, N.S. Ramgir, S. Gosavi, A.K. Debnath, *Mater. Sci. Semicond. Process.* (2022). <https://doi.org/10.1016/j.mssp.2022.106706>
14. T.P. Mokoena, H.C. Swart, D.E. Motaung, *J. Alloys Compd.* (2019). <https://doi.org/10.1016/j.jallcom.2019.06.329>
15. S.T. Navale, Z.B. Yang, C. Liu, P.J. Cao, V.B. Patil, N.S. Ramgir, R.S. Mane, F.J. Stadler, *Sens. Actuators B* (2018). <https://doi.org/10.1016/j.snb.2017.08.186>
16. V. Gerbreder, M. Krasovska, E. Sledevskis, A. Gerbreder, I. Mihailova, E. Tamanis, A. Ogurcovs, *CrystEngComm* (2020). <https://doi.org/10.1039/c9ce01556f>
17. G. Taka, T.D. Das, *IOP Conf. Ser. Earth Environ. Sci.* (2022). <https://doi.org/10.1088/1755-1315/1042/1/012017>
18. P. Rai, W.K. Kwak, Y.T. Yu, A.C.S. Appl. Mater. Interfaces. (2013). <https://doi.org/10.1021/am302811h>
19. K. Wu, L. Zhou, C. Mao, Y.J. Chu, *Mater. Lett.* (2023). <https://doi.org/10.1016/j.matlet.2023.134161>
20. Ü. Özgür, Y.I. Alivov, C. Liu, A. Teke, M.A. Reshchikov, S. Doğan, V. Avrutin, S.J. Cho, H. Morkoç, *J. Appl. Phys.* **98**, 041301 (2005)
21. H. Yang, Q. Tao, X. Zhang, A. Tang, J. Ouyang, *J. Alloys Compd.* (2008). <https://doi.org/10.1016/j.jallcom.2007.04.258>

22. S. Yang, G. Lei, H. Xu, Z. Lan, Z. Wang, H. Gu, *Nanomaterials* (2021). <https://doi.org/10.3390/nano11041026>
23. Y. Zhao, B.H. Liu, N. Liu, H. Yu, Y. Yang, X.T. Dong, *Sens. Actuators A* (2021). <https://doi.org/10.1016/j.sna.2021.112574>
24. R.R. Ambi, A.A. Mane, V.B. Patil, R.D. Mane, *Mater. Sci. Eng. B* **300**, 117066 (2024). <https://doi.org/10.1016/j.mseb.2023.117066>
25. D. Gu, X. Li, Y. Zhao, J. Wang, Enhanced NO₂ sensing of SnO₂/SnS₂ heterojunction-based sensor. *Sens. Actuators B* **244**, 67–76 (2017)
26. T. Sahm, A. Gurlo, N. Barsan, U. Weimar, L. Madler, Fundamental studies on SnO₂ by means of simultaneous work function change and conduction measurements. *Thin Solid Films* **490**, 43–47 (2005)
27. M. Hubner, C.E. Simion, A. Tomescu-Stanoiu, S. Pokhrel, N. Barsan, U. Weimar, Influence of humidity on CO sensing with p-type CuO thick film gas sensors. *Sens. Actuators B* **153**, 347–353 (2011)
28. A. Reghu, L. LeGore, J.F. Vetelino, R.J. Lad, B.G. Frederick, Distinguishing bulk conduction from band bending transduction mechanisms in chemiresistive metal oxide gas sensors. *J. Phys. Chem. C* **122**, 10607–10620 (2018)
29. B. Bhangare, N.S. Ramgir, A. Pathak, K.R. Sinju, A.K. Debnath, S. Jagtap, N. Suzuki, K.P. Muthe, C. Terashima, D.K. Aswal, S.W. Gosavi, A. Fujishima, Role of sensitizers in imparting the selective response of SnO₂/RGO based nanohybrids towards H₂S, NO₂ and H₂. *Mater. Sci. Semicond. Processing* **105**, 104726 (2020)
30. N.S. Ramgir, C.P. Goyal, P.K. Sharma, U.K. Goutam, S. Bhattacharya, N. Datta, M. Kaur, A.K. Debnath, D.K. Aswal, S.K. Gupta, *Sens. Actuators B* (2013). <https://doi.org/10.1016/j.snb.2013.07.052>
31. W. Melitz, J. Shen, A.C. Kummel, S. Lee, *Surf. Sci. Rep.* (2011). <https://doi.org/10.1016/j.surfrep.2010.10.001>
32. M. Keerthana, M. Ingle, T. P. Malini, R. Sangavi, *Rasayan J. Chem.* (2022). <https://doi.org/10.31788/Rjc.2022.1536745>
33. R. Al-Gaashani, S. Radiman, A.R. Daud, N. Tabet, Y. Al-Douri, *Ceram. Int.* (2013). <https://doi.org/10.1016/j.ceramint.2012.08.075>
34. H.H. Radamson, A. Hallén, I. Sychugov, A. Azarov, *Analytical Methods and Instruments for Micro-and Nanomaterials* (Springer, Berlin, 2023)
35. S. Gandla, S.R. Gollu, R. Sharma, V. Sarangi, D. Gupta, *Appl. Phys. Lett.* (2015). <https://doi.org/10.1063/1.4933304>
36. Q. Zhou, B. Xie, L. Jin, W. Chen, J. Li, *J. Nanotechnol.* (2016). <https://doi.org/10.1155/2016/6742104>
37. N. Jayababu, M. Poloju, J. Shruthi, M.V.R. Reddy, *Mater. Sci. Semicond. Process.* (2019). <https://doi.org/10.1016/j.mssp.2019.104591>
38. Z. Chen, T. Dedova, I.O. Acik, M. Danilson, M. Krunk, Nickel oxide films by chemical spray: effect of deposition temperature and solvent type on structural, optical, and surface properties. *Appl. Surf. Sci.* **548**, 149118 (2021)
39. S.A. El-Safty, *J. Colloid Interface Sci.* (2008). <https://doi.org/10.1016/j.jcis.2007.12.010>
40. V.V. Ganbavle, S.I. Inamdar, G.L. Agawane, J.H. Kim, K.Y. Rajpure, *Chem. Eng. J.* (2016). <https://doi.org/10.1016/j.cej.2015.10.052>
41. N.S. Ramgir, C.P. Goyal, D. Goyal, S.J. Patil, H. Ikeda, S. Ponnusamy, K.P. Muthe, A.K. Debnath, *Mater. Sci. Semicond. Process.* **134**, 106027 (2021). <https://doi.org/10.1016/j.mssp.2021.106027>
42. Z. Zhao, H. Yang, Z. Wei, Y. Xue, Y. Sun, W. Zhang, P. Li, W. Gong, S. Zhuiykov, J. Hu, *Sensors (Switzerland)*. (2020). <https://doi.org/10.3390/s20174754>
43. N. Kaur, D. Zappa, M. Ferroni, N. Poli, M. Campanini, R. Negrea, E. Comini, *Sens. Actuators B* **262**, 477–485 (2018). <https://doi.org/10.1016/j.snb.2018.02.042>
44. Y. Liu, G. Li, R. Mi, C. Deng, P. Gao, An environment-benign method for the synthesis of p-NiO/n-ZnO heterostructure with excellent performance for gas sensing and photocatalysis. *Sens. Actuators B Chem.* **191**, 537–544 (2014). <https://doi.org/10.1016/j.snb.2013.10.068>
45. V.S. Kamble, Y.H. Navale, V.B. Patil, N.K. Desai, S.T. Salunkhe, *J. Mater. Sci. Mater. Electron.* (2021). <https://doi.org/10.1007/s10854-020-04987-z>
46. Z. Chen, T. Dedova, N. Spalatu, N. Maticiu, M. Rusu, A. Katerski, I.O. Acik, T. Unold, M. Krunk, *Coll. Surf. A* **648**, 129366 (2022). <https://doi.org/10.1016/j.colsurfa.2022.129366>
47. F. Yang, Z. Guo, *J. Colloid Interface Sci.* **467**, 192–202 (2016). <https://doi.org/10.1016/j.jcis.2016.01.033>
48. G. Kavitha, K.T. Arul, P. Babu, *J. Mater. Sci.* **29**, 6666–6671 (2018). <https://doi.org/10.1007/s10854-018-8652-9>
49. Y.C. Liang, Y.C. Chang, *CrystEngComm* **22**, 2315–2326 (2020). <https://doi.org/10.1039/d0ce00052c>
50. B. Selvaraj, J.B.B. Rayappan, K.J. Babu, *J. Alloys Compd.* (2022). <https://doi.org/10.1016/j.jallcom.2022.165224>
51. Z. Qu, Y. Fu, B. Yu, P. Deng, L. Xing, X. Xue, *Sens. Actuators B* (2016). <https://doi.org/10.1016/j.snb.2015.08.058>
52. Q. Zhou, W. Zeng, W. Chen, L. Xu, R. Kumar, A. Umar, *Sens. Actuators B* (2019). <https://doi.org/10.1016/j.snb.2019.126870>
53. H. Liu, Z. Wang, G. Cao, G. Pan, X. Yang, M. Qiu, C. Sun, J. Shao, Z. Li, H. Zhang, *Mater. Sci. Semicond. Proc.*

- 141, 106435 (2022). <https://doi.org/10.1016/j.mssp.2021.106435>
54. Q. Zhou, W. Zeng, W. Chen, L. Xu, R. Kumar, A. Umar, Sens. Actuators B **298**, 126870 (2019). <https://doi.org/10.1016/j.snb.2019.126870>
55. A. Singh, B.C. Yadav, Results Surf. Interfaces **11**, 100103 (2023). <https://doi.org/10.1016/j.rsurfi.2023.100103>
56. X. Wang, X. Wang, X. Sui, W. Zhang, H. Jiang, G. Liu, B. Li, J. Zhou, Y. Sheng, E. Xie, Z. Zhang, Sens. Actuators B **400**, 134918 (2024). <https://doi.org/10.1016/j.snb.2023.134918>

Publisher's Note Springer Nature remains neutral with regard to jurisdictional claims in published maps and institutional affiliations.